

In situ synthesis of Z-scheme $\text{Ag}_3\text{PO}_4/\text{CuBi}_2\text{O}_4$ photocatalysts and enhanced photocatalytic performance for the degradation of tetracycline under visible light irradiation



Weilong Shi^a, Feng Guo^b, Songliu Yuan^{a,*}

^a School of Physics, Huazhong University of Science and Technology, Wuhan 430074, PR China

^b Key Laboratory of Subsurface Hydrology and Ecological Effects in Arid Region, Ministry of Education, School of Environmental Science and Engineering, Chang'an University, Xi'an 710064, PR China

ARTICLE INFO

Article history:

Received 21 December 2016

Received in revised form 2 February 2017

Accepted 18 March 2017

Available online 20 March 2017

Keywords:

Photocatalysts

Z-scheme system

Tetracycline

Environmental remediation

ABSTRACT

The $\text{Ag}_3\text{PO}_4/\text{CuBi}_2\text{O}_4$ (ACBO) composites with a small quantity of Ag_3PO_4 nanoparticles (0.5–10 wt.%) were synthesized by an *in situ* precipitation method and characterized by XRD, SEM, EDS, TEM, BET, XPS, UV–vis absorption spectra, PL, EIS and ESR analysis. Obviously, all the ACBO photocatalysts exhibited significantly enhanced photocatalytic performances. Meanwhile, ACBO with 5 wt.% content of Ag_3PO_4 (ACBO-5) showed the highest photocatalytic activity, which is around 2.79 and 2.16-fold higher than that of pristine Ag_3PO_4 and CuBi_2O_4 , respectively. The enhanced photocatalytic activity could be due to the efficient separation of photogenerated electron-hole pairs through the formation of Z-scheme system composed of Ag_3PO_4 , Ag and CuBi_2O_4 , in which a small quantity of reducible Ag nanoparticles acted as the charge transmission-bridge. Moreover, the high photocatalytic stability of as-synthesized ACBO heterojunction photocatalyst was obtained through five successive cycling experiments. Finally, a possible photocatalytic mechanism was also discussed.

© 2017 Elsevier B.V. All rights reserved.

1. Introduction

World wide tetracycline (TC) has increased dramatically to treat human and animal infections in the past decades. Meanwhile, due to the fact that TC is quite difficult to be metabolized completely by human or animal body, a large fraction of ingested TC is excreted in the stools and urine [1]. Consequently, it has been detected in different environmental compartments (soil, surface, and even drinking water), which has not only caused the increasing environmental pollution but also created serious threat to the health of human beings [2,3]. Undoubtedly, it is a matter of the utmost urgency to remove TC from water. A variety of conventional approaches, such as membrane filtration [4], adsorption [5,6] and electrochemical method [7,8], have been developed for the removal of TC in wastewaters. Nevertheless, most of these methods have been restricted owing to the efficiency costliness or sophisticated instrumentation for the treatment of TCs. Recent years, photocatalytic technology with high efficiency and low cost to degrade TC in the water by its outstanding advantages has gained more

and more attentions [9,10]. However, single-component photocatalysts (TiO_2 , ZnO , SnO_2 , etc.) often suffer from several shortcomings, such as poor quantum yield, poor visible light absorption efficiency and easily photo-induced charge combination, which result in low photocatalytic performance [11,12]. Afterwards, the utilization of composite materials in photocatalytic system has received more attention to overcome the drawbacks of single-component photocatalysts. For example, Zhu et al. synthesized the MWNTs- Bi_2WO_6 composites for almost 100% degradation of TC only within 60 min [13]. Shi et al. also fabricated $\text{Ag}/\text{AgBr}/\text{AgIn}(\text{MoO}_4)_2$ composites which exhibited a dramatic enhancement in the degradation rate of TC [14]. There is no doubt that composite photocatalytic system can be considered as a significant strategy for the treatment of TC, which would facilitate spatial separation of the photoinduced generated electrons and holes.

Nowadays, coupling of two matchable band gap semiconductors as a Z-scheme process has become a research hotspot for environmental remediation because of its considerably stronger redox capacity [15]. In the Z-scheme photocatalytic system, the more negative conduction band (CB) potential in one semiconductor provides the photogenerated electrons with high reduction power and the more positive valence band (VB) potential in the other semiconductor endows the photogenerated holes with deep oxidation

* Corresponding author.

E-mail address: yuanl@hust.edu.cn (S. Yuan).

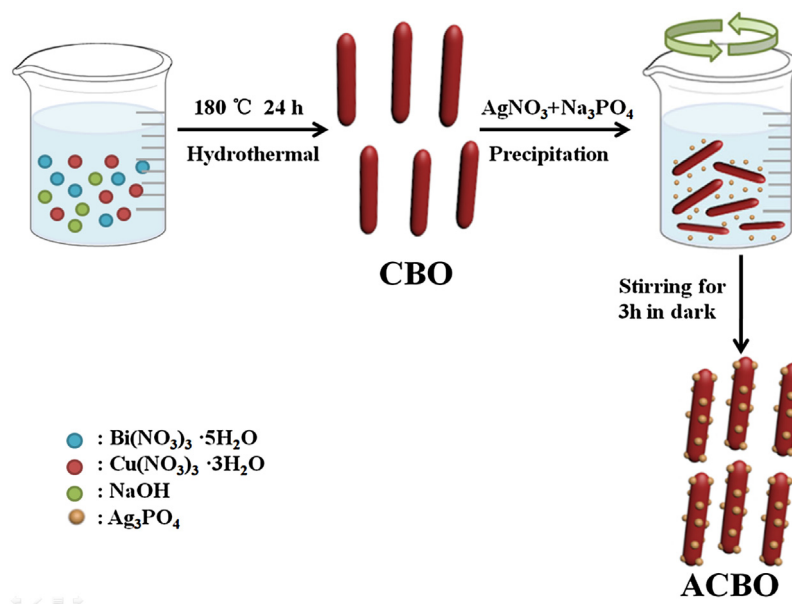


Fig. 1. Schematic illustration of the preparation for ACBO photocatalyst.

ability, resulting in the significant separation of photogenerated electron-hole pairs and further improving photocatalytic performance of single-component photocatalyst [16,17]. For instance, Jiang et al. constructed a ternary $\text{g-C}_3\text{N}_4$ - $\text{C-ZnIn}_2\text{S}_4$ nanocomposite to achieve a Z-scheme system for photocatalytic H_2 evolution, which showed significantly enhanced photocatalytic activity compared to the bare $\text{g-C}_3\text{N}_4$ and ZnIn_2S_4 [18]. Zhang et al. fabricated an effective Z-scheme $\text{BiVO}_4/\text{g-C}_3\text{N}_4$ photocatalyst for the degradation of rhodamine B, and the photocatalytic activity of 3:7 $\text{BiVO}_4/\text{g-C}_3\text{N}_4$ was as high as 10.36 and 10.68 times than that of individual $\text{g-C}_3\text{N}_4$ and BiVO_4 , respectively [19]. Therefore, it is sapiential to design Z-scheme/heterojunction photocatalysts for improving visible-light photocatalytic activity.

CuBi_2O_4 (CBO), as a novel photocatalytic material, has aroused significant research interest because of its surface catalytic and optical properties, especially for the absorption in the visible region [20–22]. Up to now, ample researches have been conducted on CBO-based heterojunction photocatalysts to allow the separation of photoinduced charge carriers in the photocatalytic field, (e.g. $\text{CuBi}_2\text{O}_4/\text{NaTaO}_3$ [23] and $p\text{-CuBi}_2\text{O}_4/n\text{-Bi}_2\text{WO}_6$ [24]). To the best of our knowledge, few researches have been reported at this point concerning CuBi_2O_4 -based Z-scheme/heterojunction photocatalysts. Ag_3PO_4 , as one of the most efficient visible-light-driven photocatalyst, presented high performances for O_2 evaluation [25] and hazardous organic contaminant degradation [26]. More recently, cooperating Ag_3PO_4 with other appropriate band-gap semiconductors to form Z-scheme heterojunction composites, which by-product Ag during the photocatalytic process is applied as a charge transmission bridge, has been proven an effective strategy to separate the photogenerated charges and prevented the reductive decomposition of Ag_3PO_4 [27]. Fortunately, CBO has suitable band edges ($E_{\text{CB}} = -0.63$ eV, $E_{\text{VB}} = 1.13$ eV) which can match well with that ($E_{\text{CB}} = 0.27$ eV and $E_{\text{VB}} = 2.67$ eV) of Ag_3PO_4 to form composite photocatalyst [28,29]. Furthermore, based on the energy level analysis, it is obvious that the gap between the CB of CuBi_2O_4 and the CB of Ag_3PO_4 is larger than that of between CB of Ag_3PO_4 and VB of CuBi_2O_4 , which indicates that the photoinduced electrons readily tend to transfer from the CB of Ag_3PO_4 to the VB of CuBi_2O_4 , then leaving rich electrons in the CB of CuBi_2O_4 and holes in the VB of Ag_3PO_4 to participate in the redox process. It is worth mentioning that in the pioneering Ag_3PO_4 containing Z-scheme composites,

(e.g. $\text{Ag}_3\text{PO}_4/\text{AgI}$ [31] and $\text{Ag}_3\text{PO}_4/\text{Ag}/\text{WO}_{3-x}$ [32]), the contents of Ag_3PO_4 are very high (more than 20 wt.%), which increased the cost of synthesized photocatalysts. Considering the practical application and cost, we deliberated to decrease the Ag_3PO_4 content and designed a novel effective and stable photocatalyst for degrading TC.

In this study, we fabricated a small quantity of Ag_3PO_4 (0.5–10 wt.%) nanoparticles to decorate on the surface of rod-like CBO for the first time by an *in situ* precipitation method. The synthesized $\text{Ag}_3\text{PO}_4/\text{CuBi}_2\text{O}_4$ (ACBO) photocatalysts possessed enhanced photocatalytic activities for the degradation of TC under visible-light irradiation compared with pure Ag_3PO_4 and CBO, and the optimal content of Ag_3PO_4 in the ACBO was also determined. Meanwhile, the photocatalytic stability of as-prepared ACBO was evaluated after five successive cycles. Furthermore, we tentatively discussed the photocatalytic mechanism of ACBO composites.

2. Experimental section

2.1. Preparation of photocatalysts

2.1.1. Synthesis of CBO

A mixture of 80 mL solution containing $\text{Bi}(\text{NO}_3)_3 \cdot 5\text{H}_2\text{O}$ (2.42 g), $\text{Cu}(\text{NO}_3)_3 \cdot 3\text{H}_2\text{O}$ (0.60 g) and NaOH (0.87 g) was stirred for 3 h at room temperature. Then, the mixed solution was put into 100 mL Teflon-lined steel autoclave and kept in an oven at 180°C for 24 h. The obtained product was washed with distilled water several times and dried in vacuum oven for 8 h at 70°C .

2.1.2. Synthesis of Ag_3PO_4 and ACBO

Ag_3PO_4 was synthesized through a facile precipitation reaction in a dark condition at room temperature. Typically, 0.3 M AgNO_3 (50 mL) was dropped into 0.1 M Na_3PO_4 (50 mL) under mild stirring. After the solution was stirred for 3 h, the obtained precipitate was collected, washed with water and dried at 70°C for 24 h.

The synthesis of ACBO hybrid photocatalysts was as follows: 0.2 g of CBO powder was dissolved into 50 mL of water, and then different volumes of AgNO_3 (0.3 M) and Na_3PO_4 (0.1 M) aqueous solution were mixed into above solution in order and stirred at room temperature for 3 h in dark. The resulted product was collected, washed with water and dried. Thus, ACBO hybrid pho-

photocatalysts with different weight ratios of Ag_3PO_4 were prepared. The weight ratios of Ag_3PO_4 in ACBO composites were 0.5%, 1%, 3%, 5% and 10% and were denoted as ACBO-0.5, ACBO-1, ACBO-3, ACBO-5 and ACBO-10, respectively.

2.2. Characterization

X-ray powder diffraction (XRD) patterns of products was recorded on an X'Pert-ProMPD/max- γ AX-ray diffractometer with Cu K α radiation ($\lambda = 0.154178$ nm). Scanning electron microscopy (SEM) images and energy dispersive X-ray analysis spectroscopy (EDS) were obtained on FEI-quanta 200 with an accelerating voltage of 20 kV. The transmission electron microscope (TEM) and high resolution transmission electron microscope (HRTEM) images were taken on FEI-Tecna F20. X-ray photoelectron spectroscopy (XPS) were carried out on an ESCALABMK II X-ray photoelectron spectrometer using Mg K α X-ray ($h\nu = 1,283.3$ eV). The UV–vis absorption spectra of as-prepared samples were performed on a Lambda 750 (Perkin-Elmer) spectrophotometer. The total organic carbon (TOC) was measured by automatic total organic carbon analyzer (TOC-V, Shimadzu, Japan). Photoluminescence (PL) study was recorded on a Fluorolog-TCSPC Luminescence Spectrometer at the excitation wavelength of 325 nm.

Electrochemical analysis was conducted on a CHI 660b workstation. The Pt wire, a calomel electrode, and the samples were served as the counter electrode, the reference electrode, and the working electrode in a three-electrode cell. Electrochemical impedance spectroscopy (EIS) was recorded by using an alternating voltage of 5 mV amplitude in the frequency range of 10^5 Hz to 10^{-2} Hz with the open circuit voltage in 0.5 M Na_2SO_4 . For transient photocurrent responses analysis, the 300 W Xe lamp (cutting off $\lambda < 420$ nm) and Na_2SO_4 (0.5 M) was employed as light source and electrolyte.

2.3. Photocatalytic activity measurement

Briefly, 50 mg photocatalyst was suspended in 100 mL aqueous solution of 10 mg/L tetracycline (TC). The solution was stirred for 30 min in dark to ensure the establishment of adsorption equilibrium. Visible light (300 W, xenon lamp) was obtained by using cut off filters to remove light of $\lambda < 420$ nm. At certain time intervals, 3 mL aliquots were extracted and centrifuged in the reaction process, then analyzed on UV–vis spectrophotometer at max wavelength of 357 nm.

2.4. Active species capturing and ESR experiments

Sacrificial agents such as 2-propanol (IPA), disodium ethylenediamine tetraacetic acid (EDTA) and 1,4-benzoquinone (BQ) were used to probe hydroxyl radicals ($\cdot\text{OH}$), holes (h^+) and superoxide radicals ($\cdot\text{O}_2^-$), respectively. This method was identical with the preceding photocatalytic activity test with the addition of 1 mmol of scavenger. In addition, the electronic spin resonance (ESR) technique was recorded on an electron paramagnetic resonance spectrometer (A300-10/12, Bruker) to further used to detect the presence of $\cdot\text{OH}$ and $\cdot\text{O}_2^-$ radicals in the photocatalytic reaction system under visible light ($\lambda > 420$ nm). The $\cdot\text{OH}$ and $\cdot\text{O}_2^-$ radicals can be captured by the DMPO. Before determining the hydroxyl radicals ($\text{DMPO}\cdot\text{OH}$) and superoxide radicals ($\text{DMPO}\cdot\text{O}_2^-$), 10 mg samples were dissolved in 0.5 mL deionized water ($\text{DMPO}\cdot\text{OH}$) or 0.5 mL methanol ($\text{DMPO}\cdot\text{O}_2^-$), and then 45 μL DMPO was added with ultrasonic dispersion for 5 min.

3. Results and discussions

In this study, we synthesized ACBO photocatalyst *via* a facile precipitation method in a dark condition at room temperature (Fig. 1).

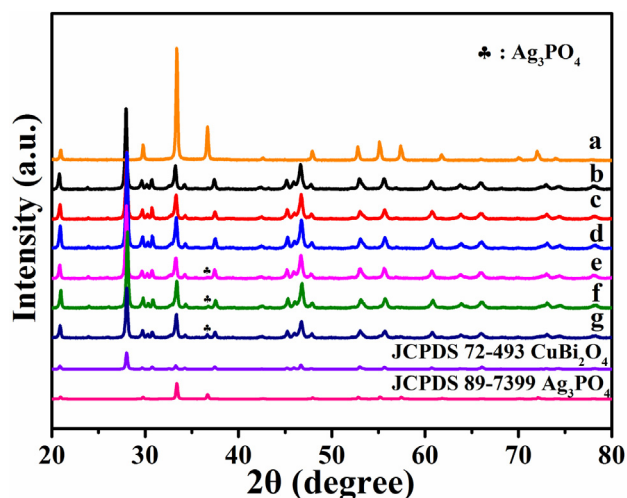


Fig. 2. XRD patterns of as-prepared samples: (a) Ag_3PO_4 , (b) CBO, (c) ACBO-0.5, (d) ACBO-1, (e) ACBO-3, (f) ACBO-5 and (g) ACBO-10.

Firstly, the CBO microrods were prepared through a hydrothermal method and dispersed in deionized water. When AgNO_3 was introduced to this dispersion, Ag^+ could be adsorbed on the surface CBO microrods. Then Na_3PO_4 as the precursor was added into the synthesis solution to form Ag_3PO_4 nanoparticles. Finally, the resulting ACBO composite is successfully obtained.

Fig. 2 shows XRD patterns of pure CBO, Ag_3PO_4 and ACBO composites with different contents of Ag_3PO_4 . As displayed in Fig. 2a and b, all the diffraction peaks of bare CBO and Ag_3PO_4 are good agreement with their monoclinic phase (JCPDS No. 72-493) and cubic phase (JCPDS No. 89-7399), respectively, demonstrating pure phases of the two samples. For ACBO composites (Fig. 2c–g), as a result of the overlapped peaks between Ag_3PO_4 and CBO as well as the quite low content of Ag_3PO_4 at the very beginning, the diffraction peaks of Ag_3PO_4 could not be detected until the content was up to 3%. Note that the main characteristic diffraction peaks of ACBO composites did not vary in peaks or shapes. The results imply a coexistence of Ag_3PO_4 and CBO, and no other impurities are found in these patterns.

The SEM images of as-prepared CBO, Ag_3PO_4 and ACBO-5 photocatalysts are shown in Fig. 3a–c. Apparently, pure CBO photocatalysts presented rod-like morphology with around 4–6 μm in length and average 130 nm in diameter (Fig. 3a), and the surface of pure CBO was very smooth. In Fig. 3b, Ag_3PO_4 samples consisted of many spherical crystals with the diameter of about 50 nm. When Ag_3PO_4 nanoparticles were anchored on the surface of CBO microrods, the surface of ACBO got rough and the size of Ag_3PO_4 become smaller, while the morphology and the size of CBO hardly changed (Fig. 3c). This phenomenon is attributed to the pre-adsorption of silver cations onto the CuBi_2O_4 surface, limiting the growth of Ag_3PO_4 particles [33,34]. Fig. 3d presents the red rectangle region of ACBO-5 sample (Fig. 3c) corresponding to the elemental mapping images. Maps of Ag-L, P-K, Cu-K, Bi-K, and O-K demonstrate the existence of CBO and Ag_3PO_4 in the ACBO-5 composite. Meanwhile, Fig. 3e also exhibits Ag, P, Bi, Cu and O as major elements in the ACBO composite through the EDS elemental analysis.

In order to further ascertain the heterojunction structure of ACBO sample, ACBO-5 is investigated by a transmission electron microscopy (TEM). It can be seen that Fig. 4a is an enlarged TEM image of an individual ACBO-5 composite. Obviously, a number of Ag_3PO_4 nanoparticles distributed on the surface of CBO microrods. In Fig. 4b, the corresponding high-resolution TEM (HR-TEM) image of the ACBO-5 sample is shown clearly resolved different lattice spacing of 0.244 nm and 0.239 nm, which corresponds to the

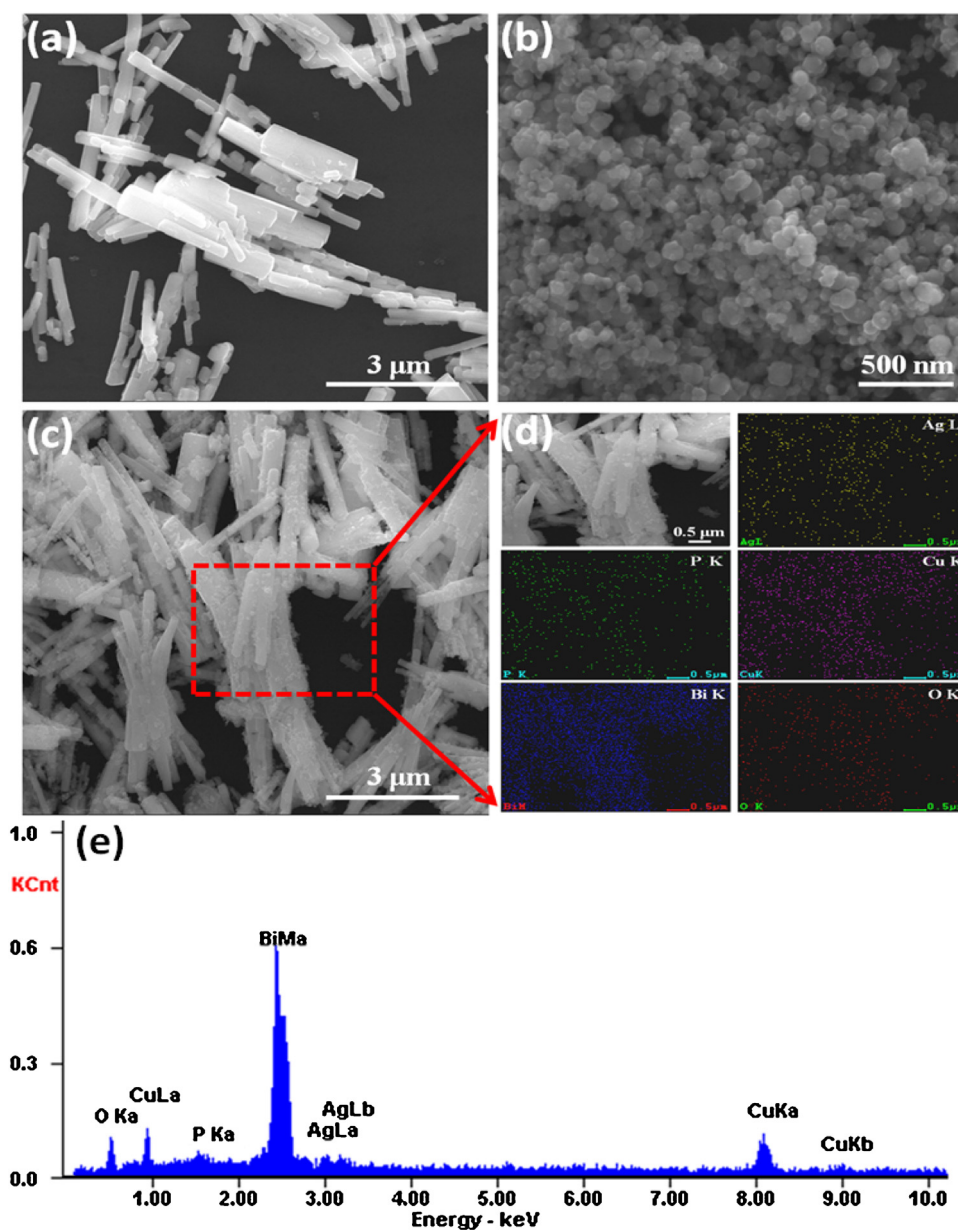


Fig. 3. SEM images of pure CBO (a), pure Ag_3PO_4 (b) and ACBO-5 (c), the corresponding elemental mapping images (d) and the EDS of ACBO-5 (e).

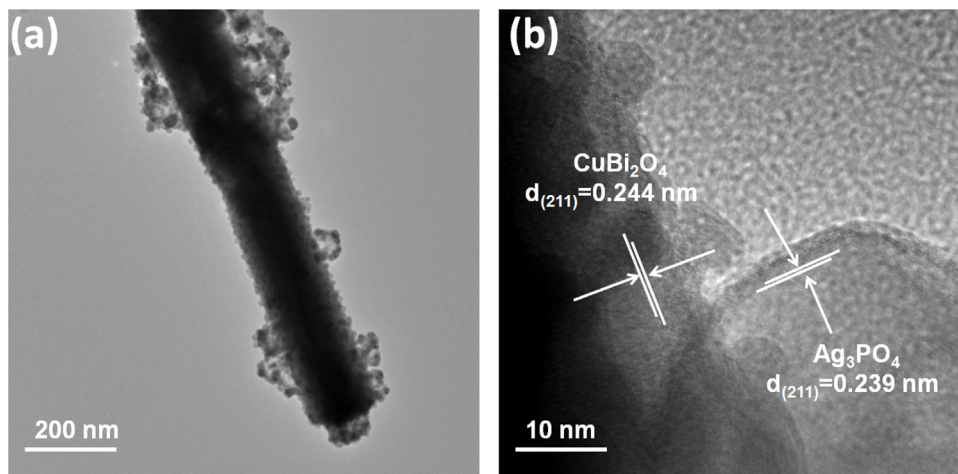


Fig. 4. TEM (a) and HR-TEM (b) image of an individual ACBO-5 composite.

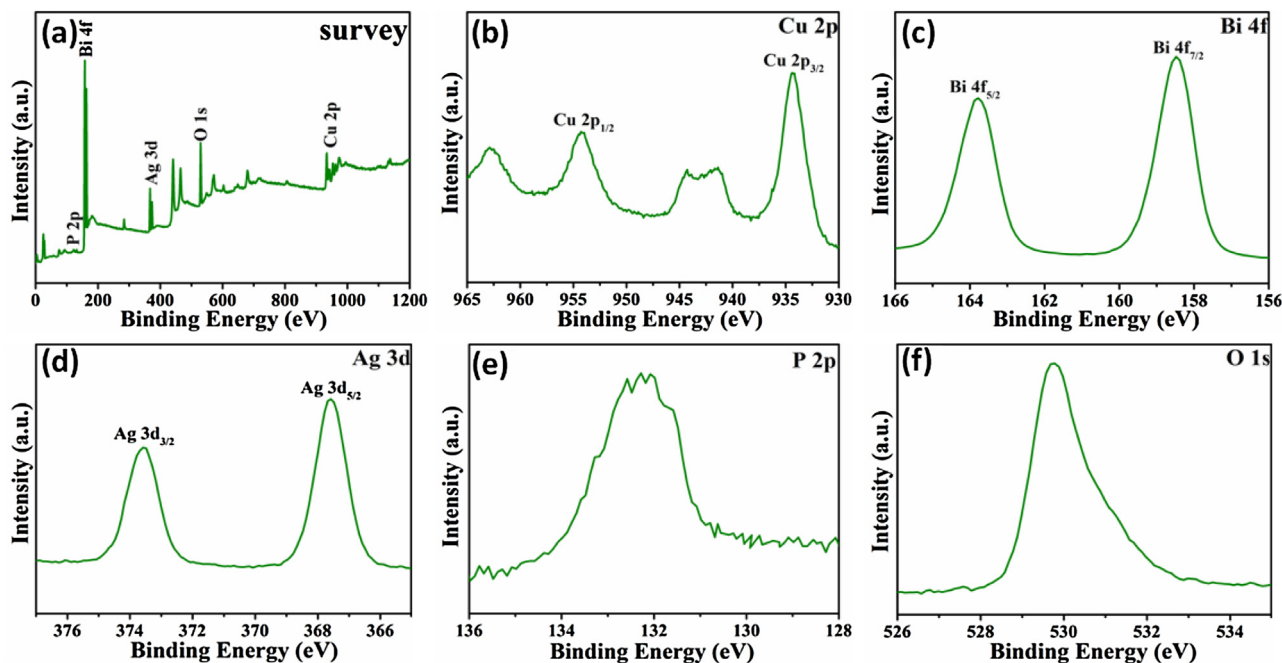


Fig. 5. XPS spectra of the ACBO-5 sample: (a) survey spectrum; (b) Cu 2p; (c) Bi 4f; (d) Ag 3d; (e) P 2p and (f) O 1s.

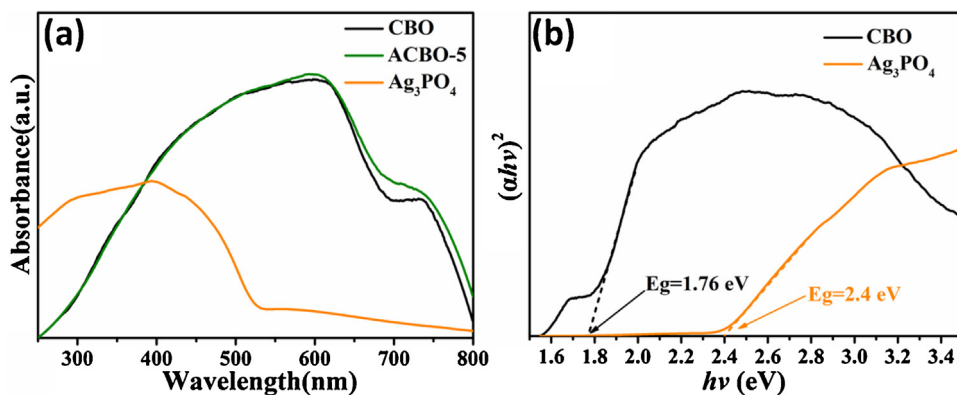


Fig. 6. (a) UV-vis DRS of as-synthesized CBO, Ag_3PO_4 and ACBO-5 samples. (b) Plots of $(\alpha h\nu)^2$ versus photon energy ($h\nu$) for the band gap energies of CBO and Ag_3PO_4 .

(211) plane of CBO and (211) plane of Ag_3PO_4 , respectively [28,30]. According to the above analysis, TEM and HR-TEM images of ACBO-5 give a solid evidence for the formation of ACBO composite.

The surface chemical composition of as-prepared ACBO photocatalyst is analyzed by XPS. Fig. 5a represents the wide XPS spectrum of ACBO, which mainly consists of the elements Cu, Bi, Ag, P and O. As shown in Fig. 5b, the binding energies of Cu $2p_{3/2}$ and Cu $2p_{1/2}$ peaks are 934 and 954 eV, and such around band gap 20.0 eV between Cu $2p_{3/2}$ and Cu $2p_{1/2}$ level accords with the standard spectrum of Cu^{2+} in copper oxides. Meanwhile, the binding energies of Cu $2p_{3/2}$ and Cu $2p_{1/2}$ have two shake-up satellites at around 943 eV and 963 eV, respectively, which may correspond to the open $3d^9$ shell of Cu^{2+} ions [35]. In Fig. 5c, the peaks at 158.5 and 164 eV are attributed to Bi $4f_{7/2}$ and Bi $4f_{5/2}$ binding energies [36]. With respect to Ag 3d spectrum (Fig. 5d), the strong peaks at 367.5 eV and 373.5 eV ascribed to the Ag $3d_{5/2}$ and Ag $3d_{3/2}$ binding energies are assigned to Ag^+ of Ag_3PO_4 , while no other peaks can be detected, indicating there is no metallic Ag^0 in the as-prepared ACBO composite before photocatalytic degradation [37]. Meanwhile, in Fig. 5e, the P 2p peak located at 132.4 eV affirms the valence state of the P^{5+} in Ag_3PO_4 [29]. Additionally, the O 1s

XPS spectrum of ACBO is shown in Fig. 5f, and the peak located at 531.3 eV is the feature of lattice oxygen [27].

The optical absorption properties of as-prepared samples are shown in Fig. 6a. Obviously, both the pure CBO and Ag_3PO_4 exhibit the intense absorption bands in the visible-light region. After a low content of Ag_3PO_4 (5 wt.%) nanoparticles anchoring on the surface of CBO microrods, the absorption ability of CBO photocatalyst in the visible-light region is enhanced, which is conducive to the utilization of the solar spectrum. Simultaneously, the band gap energies (E_g) of direct transition semiconductor can be calculated according to the plot of $(\alpha h\nu)^2$ versus photon energy ($h\nu$) [38], as shown in Fig. 6b, the E_g of Ag_3PO_4 and CBO are estimated to be 1.76 and 2.4 eV, respectively.

As shown in Fig. 7a, it is noted that the adsorption-desorption equilibrium between TC and photocatalysts reaches the adsorption equilibrium within 30 min in the dark. Meanwhile, the adsorption capacity of pure Ag_3PO_4 nanoparticles exhibits higher compared with that of pure CBO and ACBO, which may be ascribed to higher BET surface area of Ag_3PO_4 (see Fig. 8a). Also, the results in Fig. 7a indicate that the surface area is not the main factor to enhance the photocatalytic performance in this work. In Fig. 7b, the blank experiment indicates that the decomposition of TC is negligible.

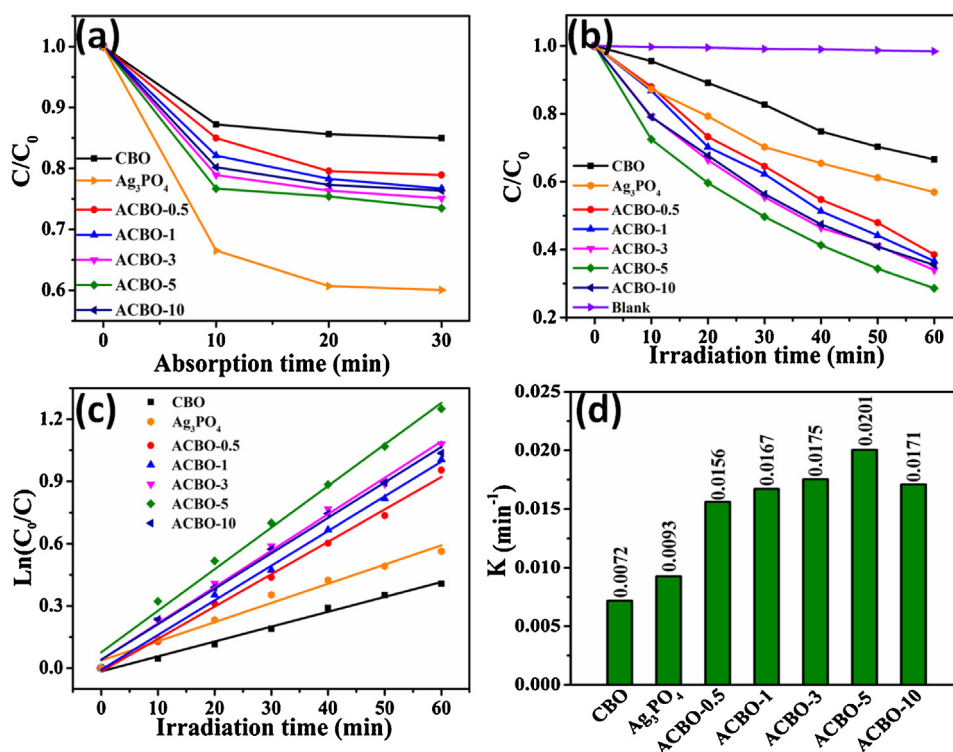


Fig. 7. (a) Absorption properties of TC over as-prepared products in the dark. (b) Photodegradations of TC over as-prepared products under visible irradiation ($\lambda > 420$ nm). (c) The pseudo-first-order reaction kinetics and (d) apparent rate constants of the prepared samples for TC degradation.

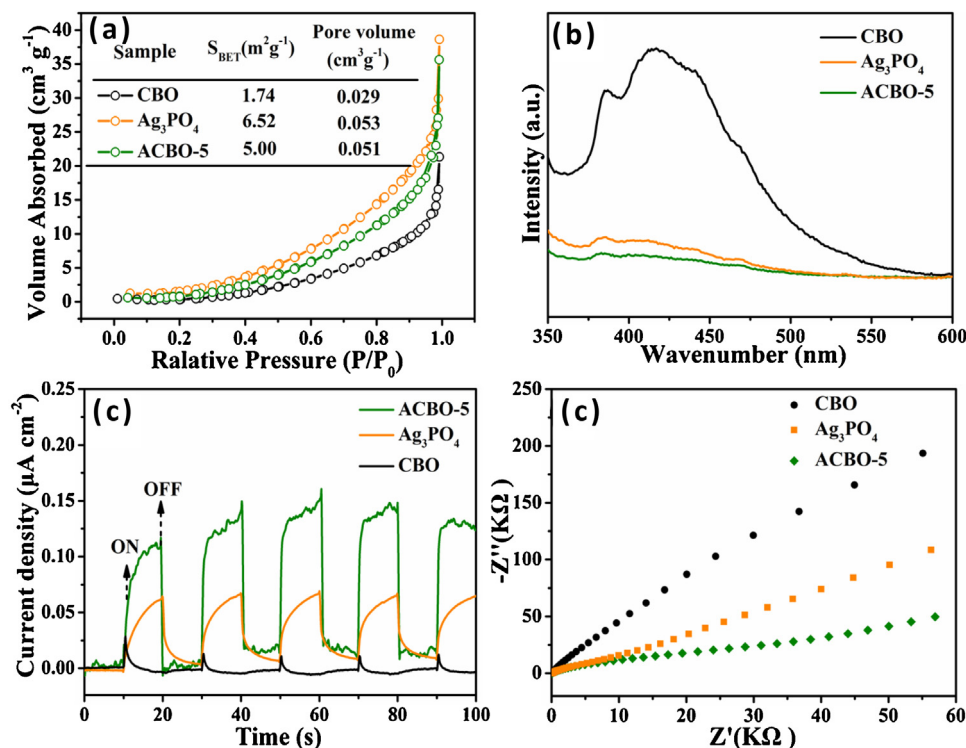


Fig. 8. (a) Nitrogen sorption isotherm and measured parameters (inset) of the as-prepared samples (b) Room temperature PL spectra of as-synthesized samples at the excitation wavelength of 325 nm; (c) Transient photocurrent responses and (d) EIS changes of ACBO-5, Ag_3PO_4 and CBO electrodes.

Additionally, pure CBO and Ag_3PO_4 displays poor photocatalytic activities, which 32% and 45% of TC were merely decomposed in 60 min under visible light irradiation, respectively. Notably, compared to pure Ag_3PO_4 and CBO, more significant degradation of

TC occurs when Ag_3PO_4 decorated on the surface of CBO micro-rods under visible-light irradiation. Moreover, with increasing the Ag_3PO_4 content, the photocatalytic activity firstly increased to a maximal value then decreased upon adding further more Ag_3PO_4

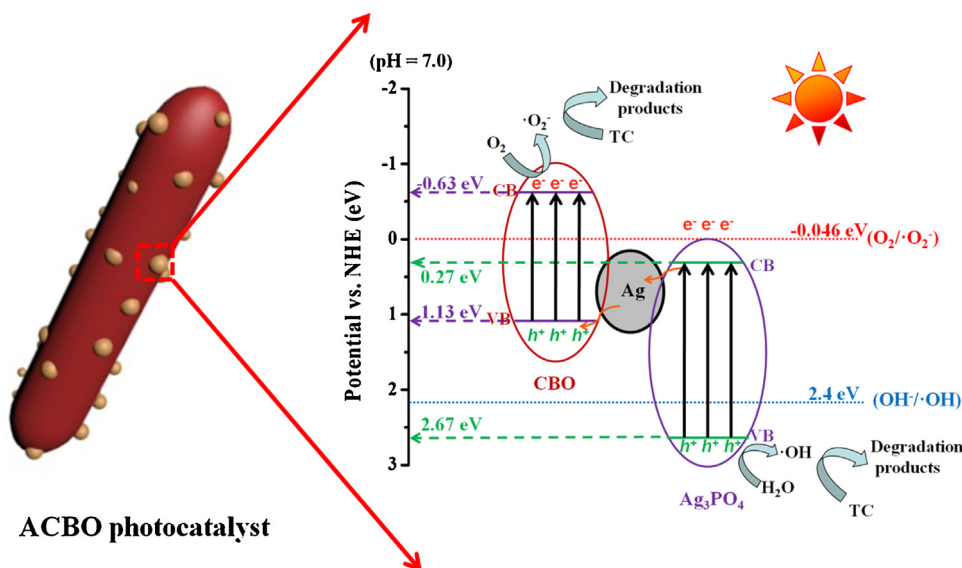


Fig. 9. Schematic diagram of photoexcited electron-hole separation process.

nanoparticles. And ACBO-5 presents the highest degradation efficiency, and nearly 75% of TC is degraded within 60 min. Fig. S1 shows the changes of characteristic absorptions of TC (at ~ 275 and 357 nm) in 60 min under the visible-light irradiation over ACBO-5. The decreased photocatalytic activity of ACBO-10 can be attributed to the excessive Ag_3PO_4 nanoparticles on the surface of CBO microrods, which may cause poor dispersion and agglomeration, further leading to the decreased photocatalytic activity. Furthermore, Fig. 7c and d display that the photocatalytic activities of TC on different catalysts $\ln(C_0/C) = kt$ and the slope k is the apparent reaction rate constant. In Fig. 7c, all the as-prepared samples follow the first order kinetics when degrading TC, and k values for all ACBO samples are obviously higher than that of Ag_3PO_4 and CBO. Fig. 7d displays that the k value of ACBO-5 (0.0201 min^{-1}) is about 2.79 and 2.16 folds compared with that of CBO (0.0072 min^{-1}) and Ag_3PO_4 (0.0093 min^{-1}), respectively. Accordingly, the results indicate that when CBO microrods were decorated with Ag_3PO_4 nanoparticles to form ACBO composite, which could greatly enhance the photocatalytic efficiency compared with either of the single sample. In addition, to further demonstrate the mineralization index of TC in the photocatalytic process, the evolution of total organic carbon (TOC) under visible light irradiation was investigated. As shown in Fig. S2, it can be seen that only 0.5% TOC was removed without any photocatalysts, while 18.3% and 51.9% TOC decrease were observed using CBO and ACBO-5 composite, respectively. This indicates the ACBO composites possessed much higher mineralization efficiency for TC photodegradation than CBO.

To further understand the higher photocatalytic activity of ACBO-5 for the degradation of TC, several tests such as PL emission, photocurrent-time measurement and EIS, were applied to explore a possible reason on the basis of experimental analysis. Generally, PL analysis is mainly used to disclose the migration, transfer and separation efficiency of the photoexcited electrons and holes in semiconductors [39]. The lower PL intensity is, the smaller recombination rate of electron-hole pairs of the photocatalyst is. Fig. 8b displays the PL spectra of pure CBO, Ag_3PO_4 and ACBO-5 composite with the excitation at 325 nm. It can be seen that the main emission peak is centered at about 410 nm for the pure CBO sample. And Ag_3PO_4 shows weak emission peaks in the range of 350–450 nm. In the PL spectrum of ACBO-5, the PL emission intensity of ACBO-5 is rapidly weakened compared with that of CBO and Ag_3PO_4 , which inhibits the recombination of photogenerated electron-hole pairs

by the introduction of Ag_3PO_4 . Moreover, the photocurrent measurements of pure CBO, Ag_3PO_4 and ACBO-5 composite are shown in Fig. 8c. All the samples possess relatively stable photocurrent responses. Significantly, ACBO-5 photocatalyst exhibits the highest photocurrent, further indicating effective separation of the photo-generated electrons and holes at the interface between Ag_3PO_4 and CBO. EIS Nyquist plots are also performed to affirm the advantage of ACBO-5 over CBO and Ag_3PO_4 sample in the process of charge separation and electron transfer. The results in Fig. 8d indicate the remarkably smallest arc was observed for ACBO-5 as compared to that of CBO and Ag_3PO_4 , which is the evidence of more effective separation of electron-hole pairs for the ACBO-5 electrodes. In addition, the EIS of ACBO-5 sample in both light irradiation and dark conditions (Fig. S3), compared with the plot obtained in the dark, a much smaller radius was obtained under irradiation, consistent with the increased electron conductivity of the electrode under visible light.

Based on the above experimental results and characterization analysis, a possible photocatalytic mechanism of the ACBO heterojunction photocatalyst is proposed as illustrated in Fig. 9. And the band-gap potentials for the CB and VB potentials of Ag_3PO_4 and CBO are calculated through the equations below:

$$E_{\text{VB}} = X - E^e + 0.5E_g \quad (1)$$

$$E_{\text{CB}} = E_{\text{VB}} - E_g \quad (2)$$

where X is the electronegativity of the semiconductor, which is the geometric average of the absolute electronegativity of the constituent atoms (Ag_3PO_4 for 5.97 eV and CBO for 4.59 eV, respectively); E^e is the energy of free electrons on the hydrogen scale ($E^e \approx 4.5 \text{ eV}$), and E_g is the band gap energy of the semiconductor. Through the calculation, the VB and CB potentials of Ag_3PO_4 are around 2.67 and 0.27 eV, which is both more positive than that of CBO (1.13 and -0.63 eV), respectively. It can be seen that the gap (0.9 eV) for the photoexcited electrons from the CB of CBO to the CB of Ag_3PO_4 is larger than the gap (0.86 eV) from the photoexcited electrons the CB of Ag_3PO_4 to the VB of CBO. Additionally, a small quantity of Ag nanoparticles occurred on the surface of Ag_3PO_4 at this early stage of visible light illumination, and the Fermi level of metallic Ag is just between the CB of Ag_3PO_4 and the VB of CBO, which acts as the charge transmission bridge. Under visible light irradiation, when the electrons can be excited from VB of both Ag_3PO_4 and CBO to the separable CB, leaving holes in both of VBs, the photoexcited electrons in the CB of Ag_3PO_4 more easily shift to

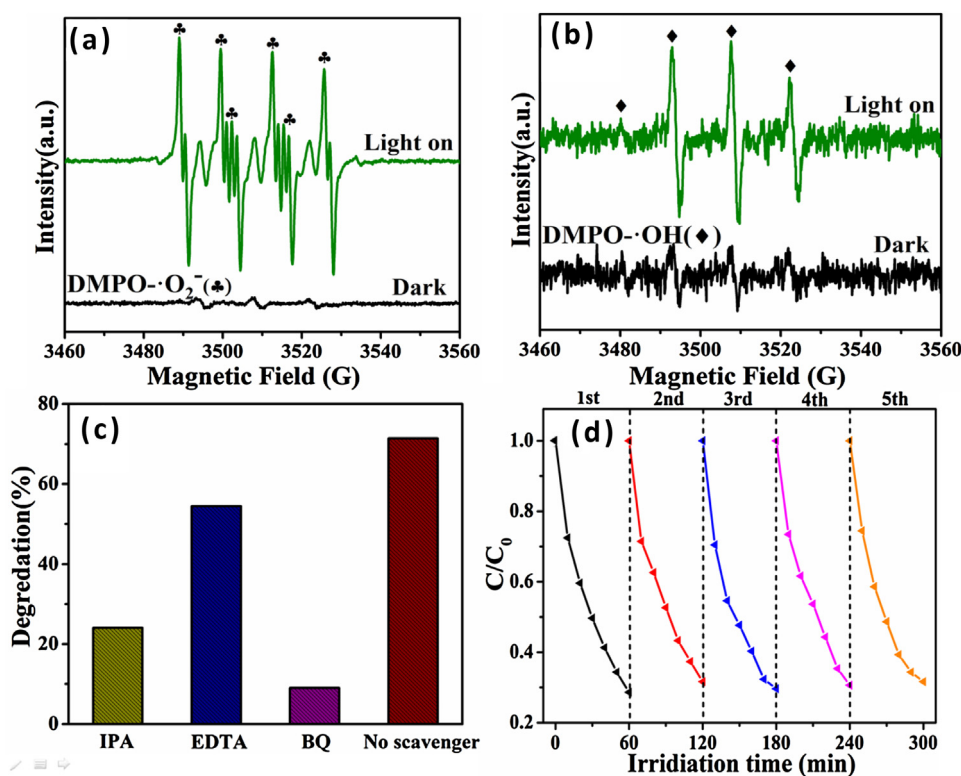


Fig. 10. (a) and (b) ESR spectra of ACBO in water and in methanol aqueous dispersion with or without visible light irradiation ($\lambda > 420$ nm). (c) Effects of a series of scavengers on the TC over ACBO. (d) Cycling runs for the photocatalytic TC degradation in the presence of ACBO-5 photocatalyst.

the metallic Ag, and subsequently transfer to CBO, then finally combine with the hole stemming from the VB of CBO. This structure is helpful for the ACBO composite to form a Z-scheme photocatalytic mechanism for the degradation of TC. Beyond that, the CB potential of CBO is more negative than the standard reduction potential of O_2/O_2^- (-0.046 eV) [19], implying the photogenerated electrons in the CB of CBO can directly reduce dissolved O_2 to O_2^- , while the photoinduced holes leaving the VB of Ag_3PO_4 can combine with OH to produce more rich active OH with powerful oxidation in the solution due to the VB potential (2.67 eV) of Ag_3PO_4 more positive than the standard reduction potential of OH/OH (2.4 eV) [19]. Therefore, the photocatalytic activity of ACBO are mainly attributed to the generated O_2^- and OH active species, meanwhile, parts of h^+ can also directly degrade TC.

In order to further elucidate our suppositional photocatalytic mechanism of ACBO composite, we also used separately ESR characterization (Fig. 10a and b) and the trapping experiments (Fig. 10c) to detect the main active species during the photocatalytic process. Obviously, the characteristic signals of the DMPO- O_2^- (Fig. 10a) and DMPO- OH (Fig. 10b) were observed under the visible light irradiation compared with ACBO in the dark. Therefore, it can be concluded that the O_2^- and OH take important roles in photodegradation process. Meanwhile, the same result was also confirmed by the trapping experiments in Fig. 10c. The degradation behavior of TC decreased slightly from 73% to 55% after adding EDTA, indicating h^+ was not the main active specie in the photocatalytic process. However, when IPA and BQ were added, the TC degradation rates rapidly decreased to 24.9% and 9.7%, which also indicated that OH and O_2^- play critical roles for degradation of TC. Thus, it is confirmed that OH and O_2^- are the main active species in the photocatalytic degradation of TC, which is just consistent with the proposed photocatalytic mechanism. From the view of the practical application, the stability of photocatalysts is a

crucial factor. Therefore, the stability of ACBO-5 photocatalyst was measured through five successive cycling experiments (Fig. 10d). Not difficult to discover, the photocatalytic activity did not exhibit any significant loss after five recycling runs, indicating that the ACBO-5 composite possesses excellent photocatalytic stability. In addition, by observing the XRD patterns of ACBO-5 before (fresh sample) and after five successive photocatalytic reaction (Fig. S4a), we found no peaks assigned to Ag^0 , which may be due to the tiny content of Ag_3PO_4 (5 wt.%) in the used ACBO-5 composite. Again, we compared with the high resolution XPS Ag 3d spectra of fresh and used ACBO-5 sample. As shown in Fig. S4b, the Ag 3d binding energy of the used ACBO-5 (Fig. S4b) increased slightly owing to the Ag^0 formation, which the weaker peaks at 368.7 eV (Ag $3d_{5/2}$) and 374.7 eV (Ag $3d_{3/2}$) are attributed to Ag^0 [40], indicating a spot of Ag^+ from Ag_3PO_4 in the ACBO has transferred to Ag^0 during the photocatalytic degradation of TC.

4. Conclusions

The ACBO Z-scheme photocatalysts have been synthesized successfully through an *in situ* precipitation method. All the ACBO photocatalysts exhibited outstanding photocatalytic activities than that of individuals for degradation of TC under visible light irradiation. The enhanced photocatalytic activity of ACBO could correspond to the formation of Z-scheme system composed of Ag_3PO_4 , Ag and CBO, which was propitious to more efficient separation of photogenerated carriers. The possible Z-scheme photocatalytic mechanism of the photocatalysts was supported by a series of experimental results. Furthermore, ACBO composite possessed good stability under visible light irradiation. This work may provide a Z-scheme composite photocatalytic system into the development and design efficient photocatalysts for environmental remediation.

Acknowledgement

This work was supported by the National Natural Science Foundation of China (11174092, 11474111).

Appendix A. Supplementary data

Supplementary data associated with this article can be found, in the online version, at <http://dx.doi.org/10.1016/j.apcatb.2017.03.048>.

References

- [1] Sh. Murphy, C. Saurel, A. Morrissey, J. Tobin, M. Oelgemoller, K. Nolan, *Appl. Catal. B* 119–120 (2012) 156–165.
- [2] E. Elmolla, M. Chaudhuri, *J. Hazard. Mater.* 170 (2009) 666–672.
- [3] M.H. Khan, H. Bae, J.Y. Jung, *J. Hazard. Mater.* 181 (2010) 659–665.
- [4] C.L. Ai, D.D. Zhou, Q. Wang, X.W. Shao, Y.J. Lei, *Sol. Energy* 113 (2015) 34–42.
- [5] L. Zhang, X. Song, X. Liu, *Chem. Eng. J.* 178 (2011) 26–33.
- [6] L. Peng, Y. Ren, J. Gu, P. Qin, Q. Zeng, J. Shao, M. Lei, L. Chai, *Environ. Sci. Pollut. Res.* 21 (2014) 7631–7640.
- [7] J. Wu, H. Zhang, N. Oturan, Y. Wang, L. Chen, M.A. Oturan, *Chemosphere* 87 (2012) 614–620.
- [8] R. Daghrir, P. Drogui, *Environ. Chem. Lett.* 11 (2013) 209–227.
- [9] A.N. Banerjee, *Nanotechnol. Sci. Appl.* 4 (2011) 35–65.
- [10] K. Nakata, A. Fujishima, *J. Photochem. Photobiol. C: Photochem. Rev.* 13 (2012) 169–189.
- [11] M.J. Munoz-Batista, M.D.L. Milagros Ballari, A. Kubacka, A.E. Cassano, O. M. Alfano, M. Fernandez-Garcia, *Chem. Eng. J.* 255 (2014) 297–306.
- [12] J. Li, S. Lv, Y. Liu, J. Bai, B. Zhou, X. Hu, *J. Hazard. Mater.* 262 (2013) 482–488.
- [13] L.F. Yue, S.F. Wang, G.Q. Shan, W. Wu, L.W. Qiang, L.Y. Zhu, *Appl. Catal. B* 176–177 (2015) 11–19.
- [14] X. Yan, X.Y. Wang, W. Gao, M.M. Wu, Y. Yan, B. Hua, G.B. Che, D.L. Han, J.H. Yang, W.Q. Fan, W.D. Shi, *Appl. Catal. B* 164 (2015) 297–304.
- [15] H. Tada, T. Mitsui, T. Kiyonaga, T. Akita, K. Tanaka, *Nat. Mater.* 5 (2006) 782–786.
- [16] H.J. Yun, H. Lee, N.D. Kim, D.M. Lee, S.J. Yu, J. Yi, *ACS Nano* 5 (2011) 4084–4090.
- [17] H.Y. Li, Y.J. Sun, B. Cai, S.Y. Gan, D.X. Han, L. Niu, T.S. Wu, *Appl. Catal. B* 170–171 (2015) 206–214.
- [18] F.F. Shi, L. Chen, M. Chen, D.L. Jiang, *Chem. Commun.* 51 (2015) 17144–17147.
- [19] N. Tian, H.W. Huang, Y. He, Y.X. Guo, T.R. Zhang, Y.H. Zhang, *Dalton Trans.* 44 (2015) 4297–4307.
- [20] Y. Xie, Y. Zhang, G. Yang, C. Liu, J. Wang, *Mater. Lett.* 107 (2013) 291–294.
- [21] W.D. Oh, S.K. Lua, Z. Dong, T.T. Lim, *Nanoscale* 7 (2015) 8149–8158.
- [22] M. Wang, J. Zai, X. Wei, W. Chen, N. Liang, M. Xu, R. Qi, X. Qian, *CrystEngComm* 17 (2015) 4019–4025.
- [23] Y.Y. Deng, Y.J. Chen, B.G. Chen, J.H. Ma, J. Alloy. *Compd.* 559 (2013) 116–122.
- [24] M. Nishikawa, S. Hiura, Y.F. Mitani, Y. Nosaka, *J. Photochem. Photobiol. A* 262 (2013) 52–56.
- [25] Z.G. Yi, J.H. Ye, N. Kikugawa, T. Kako, S.X. Ouyang, H. Stuart-Williams, H. Yang, J.Y. Cao, W.J. Luo, Z.S. Li, Y. Liu, R.L. Withers, *Nat. Mater.* 9 (2010) 559–564.
- [26] Y.P. Bi, H.Y. Hu, S.X. Ouyang, G.X. Lu, J.Y. Cao, J.H. Ye, *Chem. Commun.* 48 (2012) 3748–3750.
- [27] Z.H. Chen, F. Bing, Q. Liu, Z.G. Zhang, X.M. Fang, *J. Mater. Chem. A* 3 (2015) 4652–4658.
- [28] A. Muthukrishnaraj, S. Vadivel, I. Madejoni, N. Balasubramanian, *Ceram. Int.* 41 (2015) 6164–6168.
- [29] X. Lin, J. Hou, S.S. Jiang, Z. Lin, M. Wang, G.B. Che, *RSC Adv.* 5 (2015) 104815–104821.
- [30] X. Lin, X.Y. Guo, W.L. Shi, F. Guo, H.J. Zhai, Y.S. Yan, Q.W. Wang, *Catal. Commun.* 66 (2015) 67–72.
- [31] Z.H. Chen, W.L. Wang, Z.G. Zhang, X.M. Fang, *J. Phys. Chem. C* 117 (2013) 19346–19352.
- [32] Y.Y. Bu, Z.Y. Chen, C.J. Sun, *Appl. Catal. B* 179 (2015) 363–371.
- [33] X.F. Yang, H.Y. Cui, Y. Li, J.L. Qin, R.X. Zhang, H. Tang, *ACS. Catal.* 3 (2013) 363–369.
- [34] W.F. Yao, B. Zhang, C.P. Huang, C. Ma, X.L. Song, Q.J. Xu, *J. Mater. Chem.* 22 (2012) 4050–4055.
- [35] X.Y. Chen, C. Ma, X.X. Li, P. Chen, J.G. Fang, *Catal. Commun.* 10 (2009) 1020–1024.
- [36] S.Y. Wu, H. Zheng, Y.W. Lian, Y.Y. Wu, *Mater. Res. Bull.* 48 (2013) 2901–2907.
- [37] M.S. Zhu, P.L. Chen, M.H. Liu, *ACS Nano* 5 (2011) 4529–4536.
- [38] J. Tauc, *Mater. Res. Bull.* 5 (1970) 721–729.
- [39] Y.C. Lu, Y.H. Lin, T.F. Xie, S.L. Shi, H.M. Fan, D.J. Wang, *Nanoscale* 4 (2012) 6393–6400.
- [40] M.S. Zhu, P.L. Chen, M.H. Liu, *ACS Nano* 5 (2011) 4529–4536.